



Article

# Two-Dimensional Molecular Brush-Based Ultrahigh Edge-Nitrogen-Doped Carbon Nanosheets for Ultrafast Potassium-Ion Storage

Zongheng Cen, Youchen Tang, Junlong Huang, Yongqi Chen, Haozhen Yang, Dongtian Miao, Dingcai Wu \* and Shaohong Liu \*

PCFM Lab, School of Chemistry, Sun Yat-sen University, Guangzhou 510006, China; cenzh@mail2.sysu.edu.cn (Z.C.); tangych7@mail.sysu.edu.cn (Y.T.); huangjlong7@mail.sysu.edu.cn (J.H.); chenyq85@mail2.sysu.edu.cn (Y.C.); yanghz25@mail2.sysu.edu.cn (H.Y.); miaodt@mail2.sysu.edu.cn (D.M.)

\* Correspondence: wudc@mail.sysu.edu.cn (D.W.); liushh27@mail.sysu.edu.cn (S.L.)

**Abstract:** Heteroatom doping, especially nitrogen doping, has been regarded as an efficient strategy to break through the capacity limitation of carbonaceous anode materials in potassium-ion batteries (PIBs). Constructing edge-nitrogen-rich carbon skeleton with highly exposed active sites and efficient charge transfer is critical for the high performance of nitrogen-doped carbonaceous anode materials. Herein, a kind of ultrahigh edge-nitrogen (up to 16.2 at%) doped carbon nanosheets (ENCNS) has been developed by an efficient assembly of high-nitrogen-ratio melamine (MA) with polyacrylic acid grafted graphene oxide (GO-g-PAA) molecular brushes. The assembled PAA/MA structure facilitates the formation of an edge-nitrogen-rich carbon skeleton during heat treatment, while the highly conductive graphene backbone with a 2D nanomorphology enables shortened ion diffusion pathways and numerous exposed active surfaces. As a result, the ENCNS demonstrate excellent rate performance (up to 144 mAh g<sup>-1</sup> at 10 A g<sup>-1</sup>) and good cycle stability (136 and 100 mAh g<sup>-1</sup> after 400 cycles at 5 and 10 A g<sup>-1</sup>, respectively).

**Keywords:** molecular brushes; carbon nanosheets; edge-nitrogen doping; potassium-ion batteries



**Citation:** Cen, Z.; Tang, Y.; Huang, J.; Chen, Y.; Yang, H.; Miao, D.; Wu, D.; Liu, S. Two-Dimensional Molecular Brush-Based Ultrahigh Edge-Nitrogen-Doped Carbon Nanosheets for Ultrafast Potassium-Ion Storage. *Batteries* **2023**, *9*, 363. <https://doi.org/10.3390/batteries9070363>

Academic Editor: Seung-Wan Song

Received: 11 May 2023

Revised: 10 June 2023

Accepted: 26 June 2023

Published: 7 July 2023



**Copyright:** © 2023 by the authors. Licensee MDPI, Basel, Switzerland. This article is an open access article distributed under the terms and conditions of the Creative Commons Attribution (CC BY) license (<https://creativecommons.org/licenses/by/4.0/>).

## 1. Introduction

Lithium-ion batteries (LIBs) have dominated the rechargeable battery market because of the merits of high energy density, long cycle life, and environmental friendliness. However, the scarcity and the increasing cost of lithium sources have greatly limited their further application in the ever-increasing large-scale energy storage industry. In this context, various post-lithium systems have been developed [1–3]. Among them, potassium-ion batteries (PIBs) have been recently regarded as one of the promising alternatives of LIBs due to the abundant potassium resources in the Earth's crust (17,000 ppm), relatively low redox potential (−2.93 V vs. standard hydrogen electrode (SHE)), and similar attributes with LIBs [4–6]. Unfortunately, the much larger radius of K-ion (1.38 Å) than that of Li-ion (0.76 Å) inevitably brings sluggish K-ion insertion/extraction kinetics and large volume expansion for most anode materials used in LIBs, thereby leading to unsatisfied performances [7,8]. Therefore, developing high-performance anode materials for PIBs to solve the above problems is the key to realizing the commercial application of PIBs.

Up to date, various alloying and intercalating anodes, such as metals [9–11], transition-metal selenides/sulfides [12–15], and carbonaceous materials [16–20], have been developed for PIBs. Carbonaceous materials are particularly considered one of the most promising candidates owing to their low cost, high electric conductivity, and stable physical and chemical properties. Commercial graphite, although electrochemically active to K-ion insertion, suffers from a limited capacity (278 mAh g<sup>-1</sup>), poor cycling stability, and inferior rate performance [21,22]. Heteroatom doping, especially nitrogen doping, has

been demonstrated to be an efficient strategy to break through the capacity limitation of carbonaceous materials [23–25]. The introduction of heteroatoms in the carbon skeleton can not only enlarge the graphitic interlayer spacing for kinetically favorable K-ion insertion/extraction but also enable abundant electronegative defect sites for surface-induced K-ion adsorption/desorption [5,26–28]. Generally speaking, nitrogen dopants in the carbon skeleton can be divided into pyridinic nitrogen (N6), pyrrolic nitrogen (N5), and quaternary nitrogen (NQ). It has been reported that edge-nitrogen dopants (pyridinic and pyrrolic configurations) possess higher adsorption energy for K-ion than graphitic nitrogen dopants [29–31]. Thus, guaranteeing sufficient exposure of edge-nitrogen dopants and efficient charge transfer for K-ion storage are critical to achieving high electrochemical performances. Unfortunately, most of the reported nitrogen-doped carbonaceous materials are limited by low nitrogen doping contents and low edge-nitrogen ratios [8,24]. Meanwhile, these materials are often in the form of inhomogeneously large-sized nanostructures, which can result in sluggish charge/mass diffusion and limit the utility of the active sites [32–35]. More importantly, the state-of-art pyrolysis strategies for preparing edge-nitrogen-rich carbons are often carried out at relatively low temperatures, leading to poor electrical conductivity [36,37]. Therefore, it remains a major challenge to construct edge-nitrogen-rich carbonaceous materials with highly accessible active sites and fast charge transfer kinetics to achieve high K-ion storage performance.

Herein, we report a facile approach for the efficient synthesis of ultrahigh edge-nitrogen doped carbon nanosheets (ENCNS) by the assembly of high-nitrogen-ratio melamine (MA) with polyacrylic acid grafted graphene oxide (GO-g-PAA) molecular brushes. The as-constructed ENCNS possess a high nitrogen doping level (20.6 at%) and a high edge-nitrogen ratio (78.8% of total nitrogen), thereby enabling kinetically favorable Faradaic reaction with K-ions. Moreover, the two-dimensional (2D) nanostructures ensure high exposure of the edge-nitrogen active species to the bulk electrolyte. Additionally, the underlying graphene acts as a nanoscale current collector to facilitate charge transfer kinetics and boost the electrode conductivity. Benefiting from these integrated advantages, the ENCNS demonstrate excellent properties for K-ion storage, as characterized by excellent rate performance (144 mAh g<sup>-1</sup> at 10 A g<sup>-1</sup>) and good cycle stability at high current densities.

## 2. Materials and Methods

### 2.1. Synthesis of ENCNS, ENCNP, and CNS

A total of 80 mL of GO dispersion (1.25 mg mL<sup>-1</sup>, Hangzhou Gaoxi Technology Co., Ltd., Hangzhou, China), 0.1 mol of acrylic acid monomer (AA, Macklin, ≥99.0%), and 0.5 mmol of 2,2'-azobis [2-(2-imidazolin-2-yl)propane] dihydrochloride (AIBI, Macklin, 98%) were well mixed in a 100 mL Schlenk tube under N<sub>2</sub> protection and vigorous stirring. The Schlenk tube was then heated in an oil bath at 56 °C for 48 h, giving rise to GO-g-PAA molecular brushes [38]. To prepare GO-g-PAA/MA nanosheets, 60 mL of the as-obtained GO-g-PAA dispersion (6–7 mg mL<sup>-1</sup>) and melamine (MA, Macklin, 99.0%) were mixed under stirring for 14 h at 25 °C, followed by hydrothermal treatment at 110 °C for 24 h [24]. The molar ratio of -NH<sub>2</sub> groups in MA and -COOH groups in GO-g-PAA was controlled to be 5:1. Afterwards, the GO-g-PAA/MA nanosheets were heat treated in a tube furnace at 600 °C for 2 h with a heating rate of 5 °C min<sup>-1</sup> in flowing N<sub>2</sub>, leading to the target product of ENCNS. Different samples of ENCNS-x-y could be obtained by varying the molar ratio of -NH<sub>2</sub>/-COOH and the heat treatment temperature, where x represents the molar ratio of -NH<sub>2</sub>/-COOH and y represents the heat treatment temperature. The typical sample of ENCNS-5-600 in this work was simplified as ENCNS.

The high edge-nitrogen doped carbon nanoparticles (ENCNP) were prepared by assembly of free PAA chains with MA under identical conditions, followed by heat treatment at 600 °C for 2 h. Without the addition of MA, carbon nanosheets (CNS) were obtained under identical conditions.

## 2.2. Material Characterization

The nanomorphologies were visualized with field-emission scanning electron microscopy (FESEM, S-4800, Hitachi, Tokyo, Japan) and transmission electron microscopy (TEM, Tecnai G2 F20 S-Twin, FEI, Hillsboro, OR, USA). Powder X-ray diffraction (XRD) was performed on a D-MAX 2200 VPC diffractometer (Rigaku, Tokyo, Japan) with Cu-K $\alpha$  radiation. Raman spectrum was measured and collected using a Laser Micro-Raman Spectrometer (inVia Qontor, Renishaw, London, UK) with 532 nm laser excitation under ambient conditions. The pore structures of the samples were measured by AUTOSORB IQ3 Automated Gas Adsorption Analyzer (Quantachrome, FL, USA) at 77 K. The BET surface area ( $S_{BET}$ ) was analyzed by Brunauer–Emmett–Teller theory. The surface characteristics of the samples were investigated using an X-ray photoelectron spectroscopy (XPS, ESCALAB 250, Thermo Fisher Scientific, Waltham, MA, USA). Thermogravimetric analysis (TGA, TG 209F1 Libraz, NETZSCH, Selb, Germany) was carried out from room temperature to 700 °C with a ramp rate of 10 °C min<sup>-1</sup> under N<sub>2</sub> flow. The Fourier transform infrared spectra (FT-IR) at room temperature were recorded on an FT-IR spectrometer (NICOLET 6700, Thermo Fisher Scientific, Waltham, MA, USA).

## 2.3. Electrochemical Measurements

The electrochemical measurements of K-ion storage were conducted using CR2032 coin cells with pure K foil as the counter- and reference electrodes at room temperature. The cells were assembled in a glovebox filled with argon atmosphere (O<sub>2</sub> ≤ 0.5 ppm, H<sub>2</sub>O ≤ 0.5 ppm). The working electrodes were prepared by mixing the samples with carbon black (Super P) and polyvinylidene difluoride (PVDF) binder with a weight ratio of 7:2:1. The mass loading of active materials was about 0.3–0.5 mg cm<sup>-2</sup>. The electrolyte was 0.8 M KPF<sub>6</sub> in (1:1, v/v) ethylene carbonate (EC) and diethyl carbonate (DEC), which was purchased from Suzhou Duoduo Chemical Technology Co., Ltd., Suzhou, China. Cyclic voltammetry (CV) and electrochemical impedance spectroscopy (EIS) were performed on a CHI660E electrochemical workstation. The galvanostatic charge/discharge tests and the galvanostatic intermittent titration technique (GITT) were performed by using a LAND CT2001A battery tester within a cut-off voltage window of 0.01–3.0 V. Before the long-term cycling measurements, all cells were activated at 0.1 A g<sup>-1</sup> for three cycles.

## 2.4. Calculation of K-Ion Diffusion Coefficient ( $D_K$ )

The diffusion coefficients of K ions ( $D_K$ ) in ENCNS, ENCNP, and CNS electrodes were measured by the galvanostatic intermittent titration technique (GITT) with a periodic repetition of a current pulse of 0.05 A g<sup>-1</sup> for 30 min, followed by relaxation for 3 h. The dependence of diffusion coefficient on the depth of discharge/charge was calculated with the following equation [6]:

$$D_K = \frac{4}{\pi\tau} \left( m_B \frac{V_m}{M_b S} \right)^2 (\Delta E_s / \Delta E_\tau)^2 \quad (1)$$

where  $\tau$  represents the duration of the current impulse,  $m_B$  is the mass loading of the electrode material,  $S$  is the geometric area of the electrode,  $\Delta E_s$  is the quasi-thermodynamic equilibrium potential difference between before and after the current pulse,  $\Delta E_\tau$  represents the potential difference during the current pulse,  $V_m$  is the molar volume of the material, and  $M_b$  is the molar mass of carbon. The relative value of  $M_b/V_m$  can be calculated from the density of materials using the following equation [6]:

$$\rho = \frac{1}{V_{total} + 1/\rho_{carbon}} \quad (2)$$

where  $\rho$  (g cm<sup>-3</sup>) is the density of materials,  $V_{total}$  (cm<sup>3</sup> g<sup>-1</sup>) is the total pore volume analyzed from the N<sub>2</sub> adsorption/desorption test, and  $\rho_{carbon}$  is the true density of carbon (2 g cm<sup>-3</sup>).

### 3. Results and Discussion

The synthesis strategy of ENCNS is schematically illustrated in Figure 1. First, GO-g-PAA molecular brushes are prepared by directly grafting hair PAA chains on the surfaces of graphene oxide via free radical polymerization. In this process, PAA chains can be homogeneously grafted on GO surfaces by macromolecular radical addition to the reactive carbon-carbon double bonds [38]. According to the Fourier transform infrared (FT-IR) spectra, the presence of two new characteristic peaks of -CH<sub>2</sub>- groups at 2929 and 794 cm<sup>-1</sup>, along with the increased peak intensity of -C=O in carboxyl groups at 1695 cm<sup>-1</sup>, demonstrate the successful grafting of PAA chains on the surfaces of GO (Figure S1) [39]. Thermogravimetric analysis (TGA) shows that the weight percentage of grafted PAA chains is 56.0 wt% in GO-g-PAA (Figure S2). Benefiting from the strong interaction of acidic PAA with basic MA, high-nitrogen-ratio MA precursors can effectively react with the PAA chains of GO-g-PAA via the hydrothermal treatment at 110 °C, leading to the formation of 2D GO-g-PAA/MA nanosheets [24]. The peaks at 1651 and 1545 cm<sup>-1</sup> that correspond to the stretching vibration of -C=O and bending vibration of -C-N-H in -CONH-, respectively, reveal the formation of amide structures in GO-g-PAA/MA nanosheets (Figure S1) [40]. The hydrothermal procedure can greatly enhance the thermostability of GO-g-PAA/MA nanosheets, and thus enable the successful formation of ENCNS after heat treatment under the N<sub>2</sub> atmosphere at 600 °C [24].



**Figure 1.** Schematic illustration of the synthetic process of ENCNS.

Scanning electron microscopy (SEM) reveals that the GO-g-PAA molecular brushes and GO-g-PAA/MA nanosheets inherit the typical 2D morphology of GO nanosheets with smooth surfaces, suggestive of homogeneous deposition (Figure 2a,b). After heat treatment at 600 °C, the resulting ENCNS maintain the 2D sheet-like structure well with a decreased thickness (Figure 2c). Transmission electron microscopy (TEM) characterization further demonstrates the uniform deposition of a nitrogen-rich carbonaceous layer on graphene (Figure 2d). Such a 2D sheet-like structure provides an abundance of exposed active surfaces and extremely shortened charge transfer pathways. It should be noted that the hydrothermal reaction process can result in the formation of aggregated PAA/MA products without the addition of GO, giving rise to large-sized high-edge-nitrogen-doped carbon nanoparticles (ENCNP) after heat treatment (Figure S3). High-resolution TEM (HRTEM) image indicates that the ENCNP presents a turbostratically amorphous structure, while disorderly packed carbon nanodomains can be observed for ENCNS and carbon nanosheets (CNS) obtained by direct heat treatment of GO-g-PAA molecular brushes (Figures 2e and S3). Elemental mapping images demonstrate the presence and homogeneous distribution of carbon and nitrogen elements in ENCNS, confirming the successful preparation of 2D nitrogen-rich carbon nanosheets (Figure 2f-h).

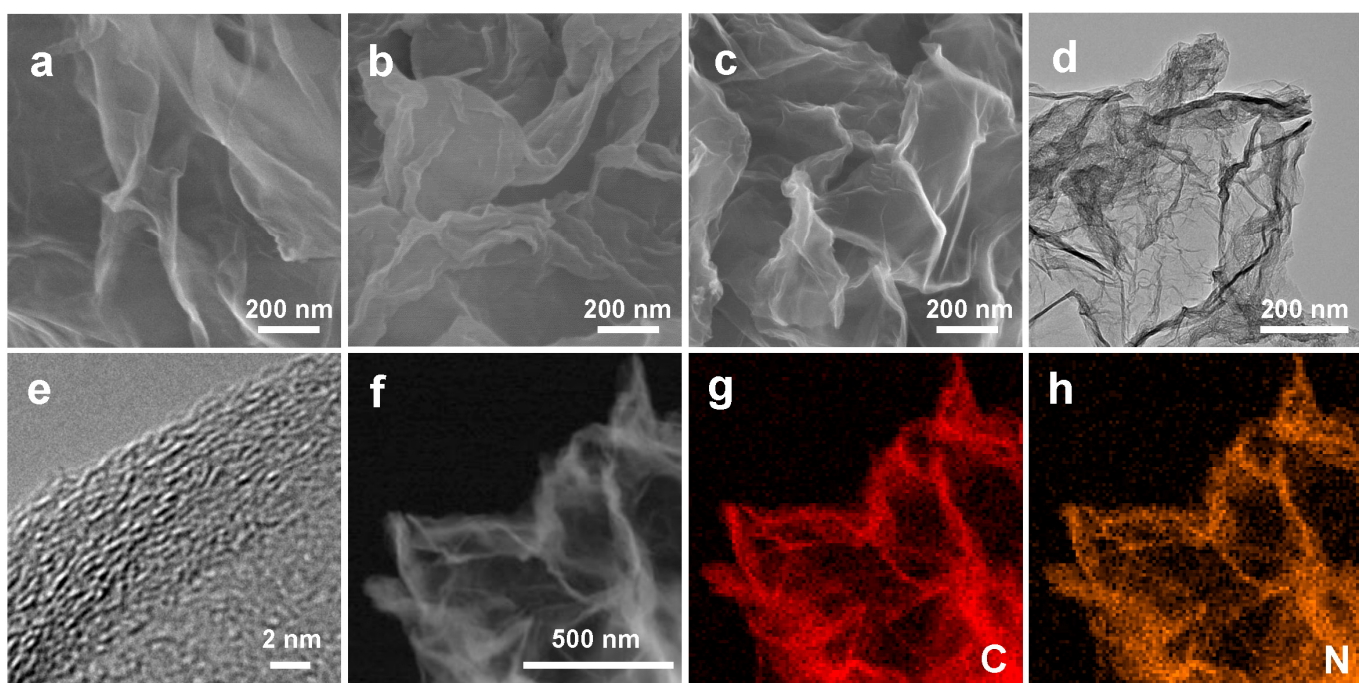


**Figure 2.** SEM images of (a) GO-g-PAA molecular brushes, (b) GO-g-PAA/MA nanosheets, and (c) ENCNS. (d) TEM, (e) HRTEM, and (f–h) elemental mapping images of ENCNS.

The X-ray diffraction (XRD) patterns in Figure 3a reveal that ENCNS, ENCPNP, and CNS exhibit broad peaks in the range of 14–36°, suggestive of amorphous structures [32]. It should be noted that ENCNS and CNS demonstrate broader half-peak widths than ENCPNP, which may be ascribed to the graphene backbone. The results agree well with the HRTEM characterization. Raman spectrum of ENCNS shows two characteristic peaks of carbon skeleton around 1350 and 1580 cm<sup>-1</sup>, which can be ascribed to disorder-induced D band and in-plane vibrational G band, respectively (Figure 3b) [41]. The much higher intensity ratios ( $I_D/I_G$ ) of ENCNS (2.51) and ENCPNP (2.63) than that of CNS suggest a disordered structure with many defects in the nitrogen-rich carbon skeletons. The N<sub>2</sub> adsorption-desorption isotherm reveals that ENCNS exhibit a hierarchical porous structure, whereas the micropores can be ascribed to the amorphous carbon derived from the PAA/MA structure on the GO and meso-/macropores result from the interspaces of aggregated carbon nanosheets (Figure 3c). The ENCNS present a high specific surface area ( $S_{BET}$ ) of 345 m<sup>2</sup> g<sup>-1</sup>, much higher than that of ENCPNP (17 m<sup>2</sup> g<sup>-1</sup>) and CNS (95 m<sup>2</sup> g<sup>-1</sup>) (Figure S4). The large surface area is beneficial for improving the accessibility of nitrogen-induced active sites, while the hierarchical porous structure can improve mass transfer.

The chemical composition of ENCNS is further investigated by X-ray photoelectron spectroscopy (XPS), demonstrating the presence of C, N, and O elements in ENCNS (Figure S5). As expected, the ENCNS display an unexpected ultrahigh nitrogen content of 20.6 at%, similar to that of ENCPNP (22.4 at%) (Table S1). The high-resolution C 1s spectrum of ENCNS demonstrates the existence of C-N bonds at 286.0 eV (Figure 3d) [23]. The high-resolution N 1s spectrum visualizes that the nitrogen species in ENCNS include pyridinic N (N6, 398.4 eV), pyrrolic N (N5, 399.8 eV), quaternary N (NQ, 401.1 eV), and oxidized N (NO, 403.2 eV), respectively (Figure 3e) [8,30,42]. According to the peak fitting results, the relative ratios of N6, N5, NQ, and NO for ENCNS are 41.1%, 37.7%, 13.4%, and 7.8%, respectively, indicating a high edge-nitrogen doping (N6 and N5) ratio of up to 78.8%. Benefiting from the high nitrogen content and the high edge-nitrogen ratio, the ENCNS demonstrate an ultrahigh edge-nitrogen content of 16.2 at%, comparable with the ENCPNP (19.6 at%) and superior to most of the previously reported N-doped carbons (Figures 3f and S6, Table S1) [27,29,43–50]. The ultra-high edge-nitrogen doping in ENCNS could provide abundant active sites and contribute to high K-ion storage capacity.

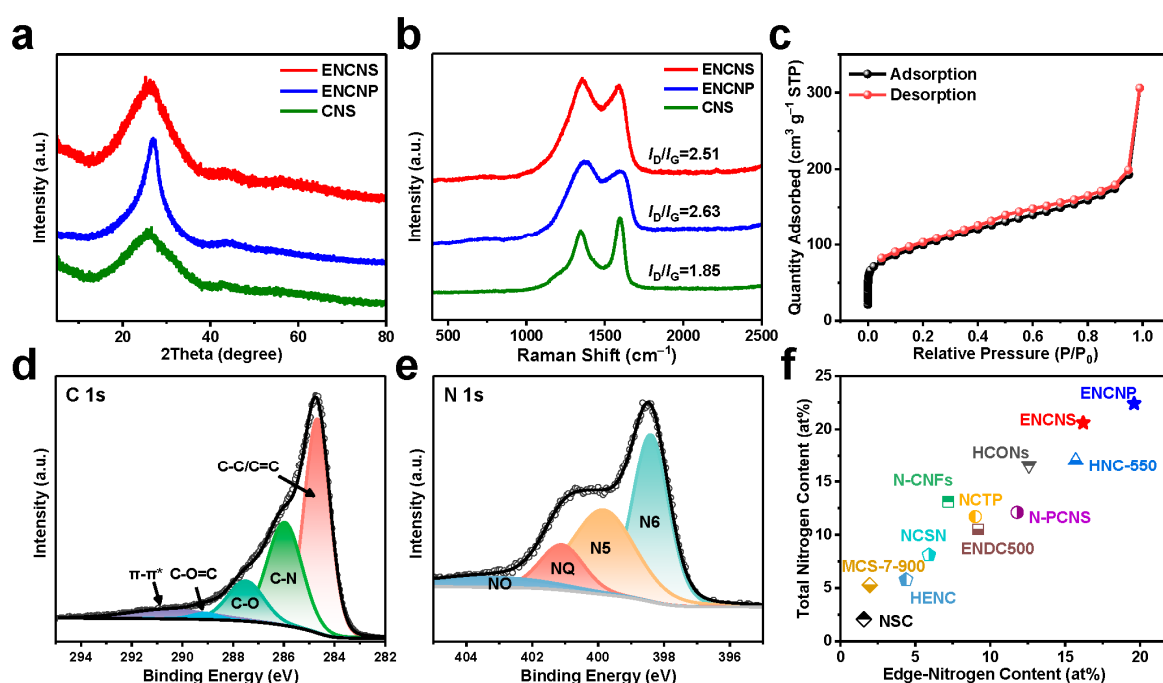


**Figure 3.** (a) XRD patterns and (b) Raman spectra of ENCNS, ENCNP, and CNS. (c)  $N_2$  adsorption-desorption isotherm of ENCNS. High-resolution (d) C 1s and (e) N 1s XPS spectra of ENCNS. (f) Total nitrogen and edge-nitrogen contents for ENCNS, ENCNP, and other reported nitrogen-doped carbon materials [27,29,43–50].

The proof-of-concept investigation into the K-ion storage properties of the ENCNS as anode materials is conducted with 0.8 M  $KPF_6$  in (1:1,  $v/v$ ) ethylene carbonate (EC) and diethyl carbonate (DEC) as the electrolytes. Figure 4a shows the cyclic voltammogram (CV) curves of the ENCNS anode between 0.01 and 3.0 V at a scan rate of  $0.2 \text{ mV s}^{-1}$  for the first three cycles. The initial cathodic scanning displays a pronounced reduction peak at around 0.49 V that disappears in subsequent cycles, which is owing to the formation of the solid electrolyte interface (SEI) layer and decomposition of the electrolyte [33]. Another small peak near the cutoff voltage is associated with the potassiation process. The broad anodic peak at 0.20–1.0 V corresponds to the depotassiation process. The CV curves overlap well in the following cycles, indicating good reversibility of the potassiation/depotassiation process. Similar results can also be observed for ENCNP and CNS anodes (Figure S7). The galvanostatic discharge/charge curves show that the initial discharge and charge capacities of ENCNS at  $0.05 \text{ A g}^{-1}$  are 1353 and  $417 \text{ mAh g}^{-1}$ , respectively, with an initial Coulombic efficiency (ICE) of 31% (Figure 4b). Similar curves and ICE can also be observed for ENCNP (32%) and CNS (15%) anodes (Figure S8). The irreversible capacity loss is frequently observed in carbonaceous materials, which can be mainly ascribed to the initial irreversible reactions such as electrolyte decomposition and formation of SEI films on the electrode surface [19,44,46,51].

Benefiting from the highly conductive 2D graphene backbone with a shortened ion diffusion length [52], the ENCNS demonstrate an excellent cycling response to a continuous variation of current densities between  $0.05$  and  $10 \text{ A g}^{-1}$ . As shown in Figure 4c, the ENCNS anode demonstrates reversible capacities of 363, 319, 295, 256, 228, 201, and  $186 \text{ mAh g}^{-1}$  when cycled at  $0.05, 0.1, 0.2, 0.5, 1, 2$ , and  $3 \text{ A g}^{-1}$ , respectively. Even at much higher current densities of  $5$  and  $10 \text{ A g}^{-1}$ , the reversible capacity of the ENCNS anode can still maintain  $168$  and  $144 \text{ mAh g}^{-1}$ , respectively, suggestive of a kinetically efficient reaction process. After switching back to  $0.1 \text{ A g}^{-1}$ , a capacity of  $307 \text{ mAh g}^{-1}$  can be recovered for repeated cycles, indicating the excellent robustness and stability of the ENCNS anode. To the best of our knowledge, such an impressive rate capability for ENCNS is superior to most of the existing KIB carbonaceous materials reported to date

(Figure 4d and Table S2) [25,43,47,50,53,54]. It should be noted that there is still a certain gap in energy density and power density between current anode materials for PIBs and mainstream anode materials for LIBs, and thus further research is needed [55]. Notably, the graphene backbone and edge-nitrogen-rich carbon layers play an important role in the high performance of the ENCNS anode. As shown in Figure 4c,d, both the nitrogen-free CNS anode and the ENCNP anode without graphene deliver much lower specific capacities under the same test conditions.

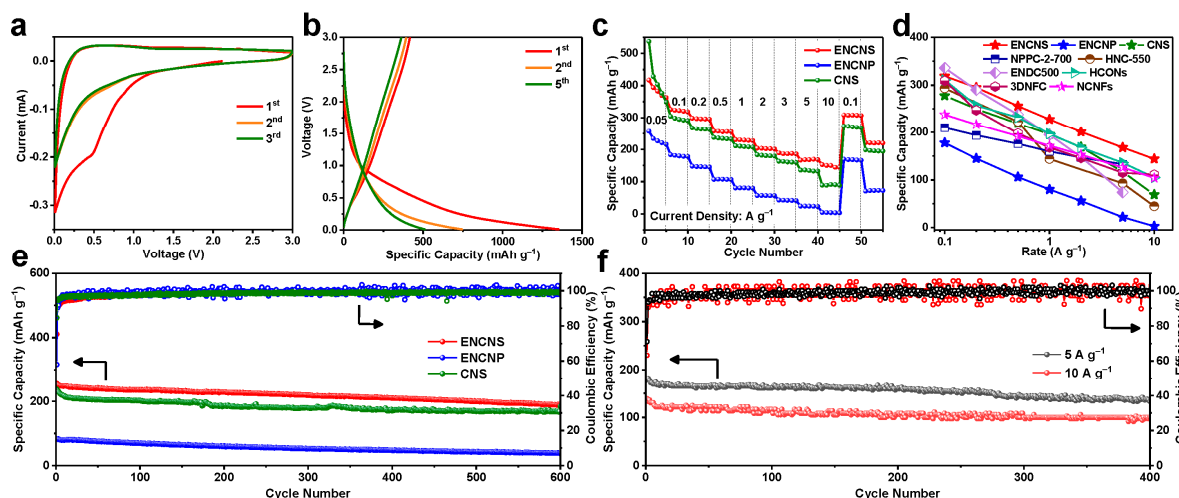


**Figure 4.** (a) CV curves of ENCNS anode at a scan rate of  $0.2 \text{ mV s}^{-1}$ . (b) Discharge/charge curves of ENCNS anode at a current density of  $0.05 \text{ A g}^{-1}$ . (c) Rate capability of ENCNS, ENCNP, and CNS anodes at various current densities between  $0.05$  and  $10.0 \text{ A g}^{-1}$ . (d) Rate capability of ENCNS, ENCNP, CNS and other reported anode materials [25,43,47,50,53,54]. (e) Long-term cycling performances of ENCNS, ENC, and CNS anodes at  $1 \text{ A g}^{-1}$ . (f) Long-term cycling performances of ENCNS anodes at  $5$  and  $10 \text{ A g}^{-1}$ .

Long-term cycling tests demonstrate that ENCNS anodes also have good stability under various current densities. As shown in Figure 4e, the ENCNS anode exhibits a capacity retention of 82% with a preserved reversible capacity of  $211 \text{ mAh g}^{-1}$  after 400 cycles at  $1 \text{ A g}^{-1}$ , along with an average Coulombic efficiency of 99.5%. In contrast, the CNS and ENCNP anodes deliver much lower reversible capacities of 171 and  $47 \text{ mAh g}^{-1}$ , respectively, after 400 cycles at  $1 \text{ A g}^{-1}$ . Even cycling at ultrahigh current densities of 5 and  $10 \text{ A g}^{-1}$ , reversible capacities of up to 136 and  $100 \text{ mAh g}^{-1}$  can still be achieved for the ENCNS anodes after 400 cycles, respectively, remarkably higher than those of CNS and ENCNP (Figures 4e and S9). It should be noted that the heat treatment temperature and mass ratio between melamine and GO-g-PAA are critical for the high performance of ENCNS anodes. A higher temperature or lower dosage of melamine can lead to decreased levels of edge-nitrogen doping, thereby resulting in inferior K-ion storage performances (Figures S10 and S11 and Table S1).

To further investigate the K-ion storage kinetics of ENCNS, CV curves at various scan rates of  $0.2$ ,  $0.4$ ,  $0.6$ ,  $0.8$ , and  $1.0 \text{ mV s}^{-1}$  between  $0.01$  and  $3.0 \text{ V}$  are obtained (Figure S12). The relationship between peak current ( $i$ ) and scan rate ( $v$ ) can be described as  $i = av^b$ . A  $b$  value of  $0.5$  suggests a diffusion-controlled electrochemical reaction, and a  $b$  value of  $1.0$  means a surface-dominated Faradaic process [54]. As shown in Figure 5a,b, the ENCNS anode exhibits higher  $b$  values than CNS and ENCNP for the anodic and cathodic peaks, suggestive of promoted capacitive K-ion storage behavior in the ENCNS anode. The capacitive contribution of the ENCNS anode can be further determined by the equation of  $i = k_1v + k_2v^{1/2}$ , in which  $k_1v$  and  $k_2v^{1/2}$  represent capacitive contribution and diffusion contribution, respectively [6,54]. As expected, the ENCNS anode demonstrates a predominately capacitive contribution of 70.7% at the scan rate of  $1.0 \text{ mV s}^{-1}$ , much higher than that of CNS (66.7%) and ENCNP (51.6%) (Figures 5c and S13). The higher capacitive

contribution of the ENCNS anode can be ascribed to the highly exposed edge-rich nitrogen sites with facilitated charge transfer. Furthermore, the galvanostatic intermittent titration technique (GITT) is performed to evaluate the K-ion diffusion behavior during the dynamic potassiation/depotassiation process (Figure S14). As shown in Figure 5d, the corresponding K-ion diffusion coefficient ( $D_K$ ) of the ENCNS anode during the whole potassiation and depotassiation process is apparently larger than that of the ENCNP anode, demonstrating enhanced K-ion diffusion kinetics in the ENCNS anode. Electrochemical impedance spectroscopy (EIS) plots further reveal that the ENCNS anode manifests a smaller charge transfer resistance ( $467 \Omega$ ) than CNS ( $788 \Omega$ ) and ENCNP ( $616 \Omega$ ) anodes (Figure 5e) [16,56]. The EIS analysis can be further generalized to estimate the  $D_K$  by using the low-frequency region of the Nyquist plots with the relationship of  $D_K = 0.5R^2T^2/A^2n^4F^2C^2\sigma^2$ , where  $R$  is the general gas constant,  $T$  is the absolute temperature,  $A$  is the surface area of electrode,  $n$  is the number of electron transferred,  $F$  is the Faraday's constant,  $C$  is the bulk concentration, and  $\sigma$  is the Warburg factor determined from the slope of  $Z'$  versus  $\omega^{-1/2}$  [18,29]. As shown in Figure 5f, the ENCNS anode has the smallest  $\sigma$  among the three samples, indicating the fastest diffusion of K-ion in the ENCNS anode.

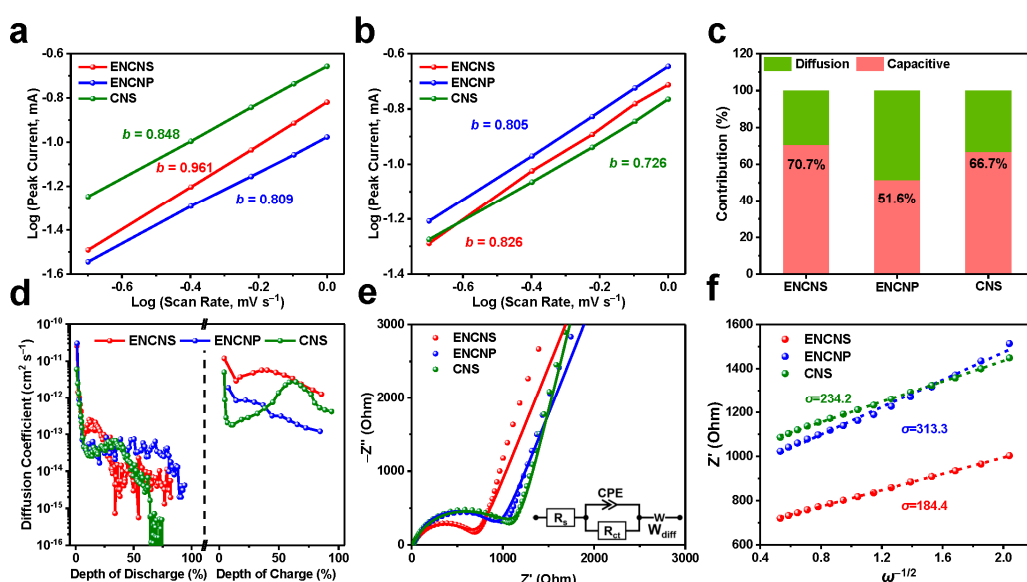


**Figure 5.** Logarithm relationship between peak currents and scan rates for ENCNS, ENCNP, and CNS anodes during the (a) depotassiation and (b) potassiation process. (c) Diffusion and capacitive contribution ratios of ENCNS, ENCNP, and CNS anodes at a scan rate of  $1.0 \text{ mV s}^{-1}$ . (d) K-ion diffusion coefficients of ENCNS, ENCNP, and CNS during the potassiation and depotassiation processes. (e) EIS plots of ENCNS, ENCNP, and CNS anodes. (f) The linear fits of the  $Z'$  versus  $\omega^{-1/2}$  in EIS plots.

#### 4. Conclusions

In summary, we have demonstrated a simple yet efficient approach to prepare a class of ultrahigh edge-nitrogen-doped carbon nanosheets as the anode materials of PIBs. The novel carbonaceous anode materials exhibit an excellent high-rate capability (up to  $144 \text{ mAh g}^{-1}$  at  $10 \text{ A g}^{-1}$ ) and long cycling times of 400 with high capacities at large current densities of 5 and  $10 \text{ A g}^{-1}$ . The superior electrochemical properties can be ascribed to the synergistic contribution of graphene-backboned 2D nanostructures and edge-nitrogen-rich carbon layers. Namely, the edge-nitrogen-rich carbon layers provide abundant active sites for surface-induced K-ion adsorption/desorption. The 2D nanostructures can facilitate the ion diffusion kinetics by shortening the pathways and increasing the accessibility of edge-nitrogen active species; meanwhile, graphene can further promote charge transfer and electrode conductivity. We hope that our present work may open up a door for the efficient preparation of edge-heteroatom-rich carbonaceous materials and offer an opportunity to

enhance their performance in various areas, such as  $I_3^-$  reduction, oxygen reduction, and hydrogen evolution.

**Supplementary Materials:** The following supporting information can be downloaded at: <https://www.mdpi.com/article/10.3390/batteries9070363/s1>. Figure S1: FT-IR spectra of GO, GO-g-PAA and GO-g-PAA/MA; Figure S2: TGA curves of GO, PAA and GO-g-PAA; Figure S3: SEM, TEM and HRTEM images of (a–c) ENCNP and (d–f) CNS; Figure S4:  $N_2$  adsorption-desorption isotherms of (a) ENCNP and (b) CNS; Figure S5: XPS full scans of ENCNS, ENCNP and CNS, revealing the presence of C, N and O elements; Figure S6: high-resolution N 1s XPS spectrum of ENCNP; Figure S7: CV curves of (a) ENCNP and (b) CNS anodes at a scan rate of  $0.2 \text{ mV s}^{-1}$ ; Figure S8: discharge/charge curves of (a) ENCNP and (b) CNS anodes at a current density of  $0.05 \text{ A g}^{-1}$ ; Figure S9: long-term cycling performances of (a) ENCNP and (b) CNS at 5 and  $10 \text{ A g}^{-1}$ ; Figure S10: rate capability of (a) ENCNS-1-600 and ENCNS-10-600 as well as (b) ENCNS-5-550 and ENCNS-5-650 at various current densities between 0.05 and  $10.0 \text{ A g}^{-1}$ ; Figure S11: high-resolution N 1s XPS spectra of (a) ENCNS-1-600, (b) ENCNS-10-600, (c) ENCNS-5-550, and (d) ENCNS-5-650; Figure S12: CV curves of (a) ENCNS, (b) ENCNP, and (c) CNS at scan rates of 0.2, 0.4, 0.6, 0.8, and  $1.0 \text{ mV s}^{-1}$ ; Figure S13: capacitive contributions of (a) ENCNS, (b) ENCNP, and (c) CNS at a scan rate of  $1.0 \text{ mV s}^{-1}$ ; Figure S14: GITT potential profiles of ENCNS, ENCNP, and CNS; Table S1: total nitrogen and edge-nitrogen contents of various samples obtained with different molar ratios of  $-\text{NH}_2$  /  $-\text{COOH}$  and heat treatment temperatures; Table S2: total nitrogen content, edge-nitrogen content, and reversible capacity at  $5 \text{ A g}^{-1}$  of ENCNS and other reported nitrogen-doped carbonaceous anode materials in PIBs [25,27,29,43–50,53,54].

**Author Contributions:** S.L. and D.W. conceived the concept and directed the research. Z.C., Y.T. and H.Y. carried out material synthesis. Z.C., J.H., Y.C., H.Y. and D.M. performed material characterization and electrochemical tests. Z.C., S.L. and D.W. wrote the paper. All authors discussed the results and commented on the manuscript. All authors have read and agreed to the published version of the manuscript.

**Funding:** This work was supported by the National Key Research and Development Program of China (2021YFF0500600), the National Natural Science Foundation of China (52172061 and 51925308), the Natural Science Foundation of Guangdong (2021A1515011617), and the Fundamental Research Funds for the Central Universities (23yxqntd002 and 23lgbj004).

**Data Availability Statement:** All data generated in this study are included in the published article and its Supplementary Materials.

**Conflicts of Interest:** The authors declare no conflict of interest.

## References

1. Hosein, I.D. The promise of calcium batteries: Open perspectives and fair comparisons. *ACS Energy Lett.* **2021**, *6*, 1560–1565. [[CrossRef](#)]
2. Zhang, T.S.; Tang, Y.; Guo, S.; Cao, X.X.; Pan, A.Q.; Fang, G.Z.; Zhou, J.; Liang, S.Q. Fundamentals and perspectives in developing zinc-ion battery electrolytes: A comprehensive review. *Energy Environ. Sci.* **2020**, *13*, 4625–4665. [[CrossRef](#)]
3. Vincent, M.; Avvaru, V.S.; Rodriguez, M.C.; Haranczyk, M.; Etacheri, V. High-rate and ultralong-life Mg-Li hybrid batteries based on highly pseudocapacitive dual-phase  $\text{TiO}_2$  nanosheet cathodes. *J. Power Sources* **2021**, *506*, 230118. [[CrossRef](#)]
4. Tu, J.W.; Tong, H.G.; Zeng, X.H.; Chen, S.; Wang, C.L.; Zheng, W.; Wang, H.; Chen, Q.W. Modification of porous N-doped carbon with sulfonic acid toward high-ICE/capacity anode material for potassium-ion batteries. *Adv. Funct. Mater.* **2022**, *32*, 2204991. [[CrossRef](#)]
5. Wang, B.; Gu, L.; Yuan, F.; Zhang, D.; Sun, H.L.; Wang, J.; Wang, Q.J.; Wang, H.; Li, Z.J. Edge-enriched N-doped graphitic carbon: Boosting rate capability and cyclability for potassium ion battery. *Chem. Eng. J.* **2022**, *432*, 134321. [[CrossRef](#)]
6. Xu, F.; Zhai, Y.X.; Zhang, E.; Liu, Q.H.; Jiang, G.S.; Xu, X.S.; Qiu, Y.Q.; Liu, X.M.; Wang, H.Q.; Kaskel, S. Ultrastable surface-dominated pseudocapacitive potassium storage enabled by edge-enriched N-doped porous carbon nanosheets. *Angew. Chem. Int. Ed.* **2020**, *59*, 19460–19467. [[CrossRef](#)]
7. Zhang, W.C.; Liu, Y.J.; Guo, Z.P. Approaching high-performance potassium-ion batteries via advanced design strategies and engineering. *Sci. Adv.* **2019**, *5*, eaav7412. [[CrossRef](#)]
8. Chu, K.N.; Zhang, X.J.; Yang, Y.; Li, Z.Q.; Wei, L.Z.; Yao, G.; Zheng, F.C.; Chen, Q.W. Edge-nitrogen enriched carbon nanosheets for potassium-ion battery anodes with an ultrastable cycling stability. *Carbon* **2021**, *184*, 277–286. [[CrossRef](#)]
9. Han, Y.; Li, T.Q.; Li, Y.; Tian, J.; Yi, Z.; Lin, N.; Qian, Y.T. Stabilizing antimony nanocrystals within ultrathin carbon nanosheets for high-performance K-ion storage. *Energy Storage Mater.* **2019**, *20*, 46–54. [[CrossRef](#)]
10. Sultana, I.; Ramireddy, T.; Rahman, M.M.; Chen, Y.; Glushenkov, A.M. Tin-based composite anodes for potassium-ion batteries. *Chem. Commun.* **2016**, *52*, 9279–9282. [[CrossRef](#)]

11. Cui, R.C.; Zhou, H.Y.; Li, J.C.; Yang, C.C.; Jiang, Q. Ball-cactus-like Bi embedded in N-riched carbon nanonetworks enables the best potassium storage performance. *Adv. Funct. Mater.* **2021**, *31*, 2103067. [[CrossRef](#)]
12. Shi, X.L.; Gan, Y.M.; Zhang, Q.X.; Wang, C.Y.; Zhao, Y.; Guan, L.H.; Huang, W. A partial sulfuration strategy derived multi-yolk-shell structure for ultra-stable K/Na/Li-ion storage. *Adv. Mater.* **2021**, *33*, 2100837. [[CrossRef](#)] [[PubMed](#)]
13. Zhang, S.P.; Ling, F.X.; Wang, L.F.; Xu, R.; Ma, M.Z.; Cheng, X.L.; Bai, R.L.; Shao, Y.; Huang, H.J.; Li, D.J.; et al. An open-ended  $\text{Ni}_3\text{S}_2\text{-Co}_9\text{S}_8$  heterostructures nanocage anode with enhanced reaction kinetics for superior potassium-ion batteries. *Adv. Mater.* **2022**, *34*, 2201420. [[CrossRef](#)] [[PubMed](#)]
14. Yang, T.; Fang, M.J.; Liu, J.W.; Yang, D.X.; Liang, Y.H.; Zhong, J.S.; Yuan, Y.J.; Zhang, Y.N.; Liu, X.L.; Zheng, R.K.; et al. Ultranarrow bandgap Se-deficient bimetallic selenides for high performance alkali metal-ion batteries. *Adv. Funct. Mater.* **2022**, *32*, 2205880. [[CrossRef](#)]
15. Hussain, N.; Li, M.X.; Tian, B.B.; Wang, H.H.  $\text{Co}_3\text{Se}_4$  quantum dots as an ultrastable host material for potassium-ion intercalation. *Adv. Mater.* **2021**, *33*, 2102164. [[CrossRef](#)]
16. Huang, H.J.; Xu, R.; Feng, Y.Z.; Zeng, S.F.; Jiang, Y.; Wang, H.J.; Luo, W.; Yu, Y. Sodium/potassium-ion batteries: Boosting the rate capability and cycle life by combining morphology, defect and structure engineering. *Adv. Mater.* **2020**, *32*, 1904320. [[CrossRef](#)]
17. Lu, Y.H.; Tang, Y.C.; Tang, K.H.; Wu, D.C.; Ma, Q. Controllable fabrication of superhierarchical carbon nanonetworks from 2D molecular brushes and their use in electrodes of flexible supercapacitors. *New Carbon Mater.* **2022**, *37*, 978–987. [[CrossRef](#)]
18. Mahmood, A.; Li, S.; Ali, Z.; Tabassum, H.; Zhu, B.J.; Liang, Z.B.; Meng, W.; Aftab, W.; Guo, W.H.; Zhang, H.; et al. Ultrafast sodium/potassium-ion intercalation into hierarchically porous thin carbon shells. *Adv. Mater.* **2019**, *31*, 1805430. [[CrossRef](#)]
19. Feng, W.C.; Wang, H.; Jiang, Y.L.; Zhang, H.Z.; Luo, W.; Chen, W.; Shen, C.L.; Wang, C.X.; Wu, J.S.; Mai, L.Q. A strain-relaxation red phosphorus free-standing anode for non-aqueous potassium ion batteries. *Adv. Energy Mater.* **2022**, *12*, 2103343. [[CrossRef](#)]
20. Liu, Y.; Lu, Y.X.; Xu, Y.S.; Meng, Q.S.; Gao, J.C.; Sun, Y.G.; Hu, Y.S.; Chang, B.B.; Liu, C.T.; Cao, A.M. Pitch-derived soft carbon as stable anode material for potassium ion batteries. *Adv. Mater.* **2020**, *32*, 2000505. [[CrossRef](#)]
21. Ling, Z.; Wang, F.Q.; Shi, C.R.; Wang, Z.Y.; Fan, X.H.; Wang, L.; Zhao, J.F.; Jiang, L.L.; Li, Y.H.; Chen, C.; et al. Fast peel-off ultrathin, transparent, and free-standing films assembled from low-dimensional materials using MXene sacrificial layers and produced bubbles. *Small Methods* **2022**, *6*, 2101388. [[CrossRef](#)] [[PubMed](#)]
22. Jian, Z.L.; Luo, W.; Ji, X.L. Carbon electrodes for K-ion batteries. *J. Am. Chem. Soc.* **2015**, *137*, 11566–11569. [[CrossRef](#)] [[PubMed](#)]
23. Lu, Y.H.; Tang, Y.C.; Liu, R.L.; Li, C.F.; Liu, S.H.; Zhu, Y.L.; Wu, D.C. Multifunctional Templating Strategy for Fabrication of Fe, N-Codoped Hierarchical Porous Carbon Nanosheets. *Chin. J. Polym. Sci.* **2022**, *40*, 2–6. [[CrossRef](#)]
24. Zhang, W.L.; Yin, J.; Sun, M.L.; Wang, W.X.; Chen, C.L.; Altunkaya, M.; Emwas, A.H.; Han, Y.; Schwingenschlogl, U.; Alshareef, H.N. Direct pyrolysis of supermolecules: An ultrahigh edge-nitrogen doping strategy of carbon anodes for potassium-ion batteries. *Adv. Mater.* **2020**, *32*, 2000732. [[CrossRef](#)]
25. Ma, X.Q.; Xiao, N.; Xiao, J.; Song, X.D.; Guo, H.D.; Wang, Y.T.; Zhao, S.J.; Zhong, Y.P.; Qiu, J.S. Nitrogen and phosphorus dual-doped porous carbons for high-rate potassium ion batteries. *Carbon* **2021**, *179*, 33–41. [[CrossRef](#)]
26. Share, K.; Cohn, A.P.; Carter, R.; Rogers, B.; Pint, C.L. Role of nitrogen-doped graphene for improved high-capacity potassium ion battery anodes. *ACS Nano* **2016**, *10*, 9738–9744. [[CrossRef](#)]
27. Zhang, D.M.; Chen, Z.W.; Bai, J.; Yang, C.C.; Jiang, Q. Highly nitrogen-doped porous carbon nanosheets as high-performance anode for potassium-ion batteries. *Batter. Supercaps* **2020**, *3*, 185–193. [[CrossRef](#)]
28. Li, Z.J.; Wu, X.F.; Luo, W.; Wang, C.X.; Feng, W.C.; Hong, X.F.; Mai, L.Q. Dual sulfur-doped sites boost potassium storage in carbon nanosheets derived from low-cost sulfonate. *Chem. Eng. J.* **2022**, *431*, 134207. [[CrossRef](#)]
29. Liu, Q.D.; Han, F.; Zhou, J.F.; Li, Y.; Chen, L.; Zhang, F.Q.; Zhou, D.W.; Ye, C.; Yang, J.X.; Wu, X.; et al. Boosting the potassium-ion storage performance in soft carbon anodes by the synergistic effect of optimized molten salt medium and N/S dual-doping. *ACS Appl. Mater. Inter.* **2020**, *12*, 20838–20848. [[CrossRef](#)]
30. Xu, Y.; Sun, X.P.; Li, Z.Q.; Wei, L.Z.; Yao, G.; Niu, H.L.; Yang, Y.; Zheng, F.C.; Chen, Q.W. Boosting the  $\text{K}^+$ -adsorption capacity in edge-nitrogen doped hierarchically porous carbon spheres for ultrastable potassium ion battery anodes. *Nanoscale* **2021**, *13*, 19634–19641. [[CrossRef](#)]
31. Jin, S.Y.; Liang, P.; Jiang, Y.T.; Min, H.H.; Niu, M.M.; Yang, H.; Zhang, R.G.; Yan, J.X.; Shen, X.D.; Wang, J. Preferentially engineering edge-nitrogen sites in porous hollow spheres for ultra-fast and reversible potassium storage. *Chem. Eng. J.* **2022**, *435*, 134821. [[CrossRef](#)]
32. Tang, Y.C.; Liu, R.L.; Liu, S.H.; Zheng, B.N.; Lu, Y.H.; Fu, R.W.; Wu, D.C.; Zhang, M.Q.; Rong, M.Z. Cobalt and nitrogen codoped ultrathin porous carbon nanosheets as bifunctional electrocatalysts for oxygen reduction and evolution. *Carbon* **2019**, *141*, 704–711. [[CrossRef](#)]
33. Chang, X.Q.; Zhou, X.L.; Ou, X.W.; Lee, C.S.; Zhou, J.W.; Tang, Y.B. Ultrahigh nitrogen doping of carbon nanosheets for high capacity and long cycling potassium ion storage. *Adv. Energy Mater.* **2019**, *9*, 1902672. [[CrossRef](#)]
34. Zhang, W.L.; Sun, M.L.; Yin, J.; Lu, K.; Schwingenschlogl, U.; Qiu, X.Q.; Alshareef, H.N. Accordion-like carbon with high nitrogen doping for fast and stable K ion storage. *Adv. Energy Mater.* **2021**, *11*, 2101928. [[CrossRef](#)]
35. Wu, X.F.; Li, Z.J.; Liu, J.X.; Luo, W.; Gaumet, J.J.; Mai, L.Q. Defect engineering of hierarchical porous carbon microspheres for potassium-ion storage. *Rare Met.* **2022**, *41*, 3446–3455. [[CrossRef](#)]
36. Wang, P.; Qi, X.H.; Zhao, W.; Qian, M.; Bi, H.; Huang, F.Q. Nitrogen-doped hierarchical few-layered porous carbon for efficient electrochemical energy storage. *Carbon Energy* **2021**, *3*, 349–359. [[CrossRef](#)]

37. Xu, J.J.; Xu, F.; Qian, M.; Xu, F.F.; Hong, Z.L.; Huang, F.Q. Conductive carbon nitride for excellent energy storage. *Adv. Mater.* **2017**, *29*, 1701674. [[CrossRef](#)] [[PubMed](#)]
38. Kan, L.Y.; Xu, Z.; Gao, C. General avenue to individually dispersed graphene oxide-based two-dimensional molecular brushes by free radical polymerization. *Macromolecules* **2011**, *44*, 444–452. [[CrossRef](#)]
39. Wang, Q.Q.; Lei, L.L.; Kang, X.Y.; Su, X.Q.; Wang, F.C.; Wang, C.; Zhao, J.H.; Chen, Z.J. Preparation of the crosslinked GO/PAA aerogel and its adsorption properties for Pb(II) ions. *Mater. Res. Express* **2020**, *7*, 025514. [[CrossRef](#)]
40. Olar, R.; Scaeteanu, G.V.; Danila, G.M.; Daniliuc, C.G.; Korosec, R.C.; Korosin, N.C.; Badea, M. Synthesis and characterization of cobalt acrylate-melamine co-crystals. *J. Therm. Anal. Calorim.* **2019**, *135*, 2257–2264. [[CrossRef](#)]
41. Liu, X.H.; Zhang, J.; Guo, S.J.; Pinna, N. Graphene/N-doped carbon sandwiched nanosheets with ultrahigh nitrogen doping for boosting lithium-ion batteries. *J. Mater. Chem. A* **2016**, *4*, 1423–1431. [[CrossRef](#)]
42. Chen, Y.Q.; Huang, J.L.; Chen, Z.R.; Shi, C.G.; Yang, H.Z.; Tang, Y.C.; Cen, Z.H.; Liu, S.H.; Fu, R.W.; Wu, D.C. Molecular engineering toward high-crystallinity yet high-surface-area porous carbon nanosheets for enhanced electrocatalytic oxygen reduction. *Adv. Sci.* **2022**, *9*, 2103477. [[CrossRef](#)]
43. Huang, R.; Cao, Y.P.; Qin, S.Y.; Ren, Y.X.; Lan, R.C.; Zhang, L.Y.; Yu, Z.; Yang, H. Ultra-high N-doped open hollow carbon nano-cage with excellent Na<sup>+</sup> and K<sup>+</sup> storage performances. *Mater. Today Nano* **2022**, *18*, 100217. [[CrossRef](#)]
44. Gong, J.; Zhao, G.Q.; Feng, J.K.; Wang, G.L.; Shi, Z.L.; An, Y.L.; Zhang, L.; Li, B. Control of the structure and composition of nitrogen-doped carbon nanofoams derived from CO<sub>2</sub> foamed polyacrylonitrile as anodes for high-performance potassium-ion batteries. *Electrochim Acta* **2021**, *388*, 138630. [[CrossRef](#)]
45. Zheng, J.F.; Wu, Y.J.; Tong, Y.; Liu, X.; Sun, Y.J.; Li, H.Y.; Niu, L. High capacity and fast kinetics of potassium-ion batteries boosted by nitrogen-doped mesoporous carbon spheres. *Nano-Micro Lett.* **2021**, *13*, 174. [[CrossRef](#)] [[PubMed](#)]
46. Bi, H.H.; He, X.J.; Yang, L.; Li, H.Q.; Jin, B.Y.; Qiu, J.S. Interconnected carbon nanocapsules with high N/S co-doping as stable and high-capacity potassium-ion battery anode. *J. Energy Chem.* **2022**, *66*, 195–204. [[CrossRef](#)]
47. Zhang, W.L.; Cao, Z.; Wang, W.X.; Alhajji, E.; Emwas, A.-H.; Costa, P.M.F.J.; Cavallo, L.; Alshareef, H.N. A site-selective doping strategy of carbon anodes with remarkable K-ion storage capacity. *Angew. Chem. Int. Ed.* **2020**, *59*, 4448–4455. [[CrossRef](#)] [[PubMed](#)]
48. Zhao, Y.; Sun, Z.T.; Yi, Y.Y.; Lu, C.; Wang, M.L.; Xia, Z.; Lian, X.Y.; Liu, Z.F.; Sun, J.Y. Precise synthesis of N-doped graphitic carbon via chemical vapor deposition to unravel the dopant functions on potassium storage toward practical K-ion batteries. *Nano Res.* **2021**, *14*, 1413–1420. [[CrossRef](#)]
49. Wang, K.; Li, N.N.; Sun, L.; Zhang, J.; Liu, X.H. Free-standing N-doped carbon nanotube films with tunable defects as a highcapacity anode for potassium-ion batteries. *ACS Appl. Mater. Inter.* **2020**, *12*, 37506–37514. [[CrossRef](#)]
50. Liu, S.T.; Yang, B.B.; Zhou, J.S.; Song, H.H. Nitrogen-rich carbon-onion-constructed nanosheets: An ultrafast and ultrastable dual anode material for sodium and potassium storage. *J. Mater. Chem. A* **2019**, *7*, 18499–18509. [[CrossRef](#)]
51. Cheng, N.; Zhou, W.; Liu, J.L.; Liu, Z.G.; Lu, B.A. Reversible oxygen-rich functional groups grafted 3D honeycomb-like carbon anode for super-long potassium ion batteries. *Nano-Micro Lett.* **2022**, *14*, 146. [[CrossRef](#)] [[PubMed](#)]
52. Wang, C.X.; Yu, R.H.; Luo, W.; Feng, W.C.; Shen, Y.H.; Xu, N.; Mai, L.Q. Chemical cross-linking and mechanically reinforced carbon network constructed by graphene boosts potassium ion storage. *Nano Res.* **2022**, *15*, 9019–9025. [[CrossRef](#)]
53. Yang, B.J.; Chen, J.T.; Liu, L.Y.; Ma, P.J.; Liu, B.; Lang, J.W.; Tang, Y.; Yan, X.B. 3D nitrogen-doped framework carbon for high-performance potassium ion hybrid capacitor. *Energy Storage Mater.* **2019**, *23*, 522–529. [[CrossRef](#)]
54. Xu, Y.; Zhang, C.L.; Zhou, M.; Fu, Q.; Zhao, C.X.; Wu, M.H.; Lei, Y. Highly nitrogen doped carbon nanofibers with superior rate capability and cyclability for potassium ion batteries. *Nat. Commun.* **2018**, *9*, 1720. [[CrossRef](#)]
55. Ben, L.B.; Zhou, J.; Ji, H.X.; Yu, H.L.; Zhao, W.W.; Huang, X.J. Si nanoparticles seeded in carbon-coated Sn nanowires as an anode for high-energy and high-rate lithium-ion batteries. *Mater. Futur.* **2022**, *1*, 015101. [[CrossRef](#)]
56. Lu, Z.X.; Wang, J.; Feng, W.L.; Yin, X.P.; Feng, X.C.; Zhao, S.Y.; Li, C.X.; Wang, R.X.; Huang, Q.A.; Zhao, Y.F. Zinc Single-Atom-Regulated Hard Carbons for High-Rate and Low-Temperature Sodium-Ion Batteries. *Adv. Mater.* **2023**, *35*, 2211461. [[CrossRef](#)]

**Disclaimer/Publisher’s Note:** The statements, opinions and data contained in all publications are solely those of the individual author(s) and contributor(s) and not of MDPI and/or the editor(s). MDPI and/or the editor(s) disclaim responsibility for any injury to people or property resulting from any ideas, methods, instructions or products referred to in the content.